sustainable chemistry

MDPI

Article

Correlation Between Conductivity and Oxygen Evolution Reaction Activity in Perovskite Oxides $CaMnO_{3-\delta}$, $Ca_{0.5}Sr_{0.5}MnO_{3-\delta}$ and $SrMnO_{3-\delta}$

Amara Martinson, Mandy Guinn, Peter Mortensen and Ram Krishna Hona *

Environmental Science Department, United Tribes Technical College, Bismarck, ND 58504, USA; martinson.amara@stu.uttc.edu (A.M.); mguinn@uttc.edu (M.G.); pmortensen@uttc.edu (P.M.)
* Correspondence: rhona@uttc.edu; Tel.: +1-(701)-221-1329

Abstract: The perovskite oxides $CaMnO_{3-\delta}$, $Ca_{0.5}Sr_{0.5}MnO_{3-\delta}$, and $SrMnO_{3-\delta}$ were synthesized in air using a solid-state method, and their structural, electrical, and electrocatalytic properties were studied in relation to their oxygen evolution reaction (OER) performance. Iodometric titration showed δ values of 0.05, 0.05, and 0.0, respectively, indicating that Mn is predominantly in the 4+ oxidation state across all materials, consistent with prior reports. Detailed characterization was performed using X-ray diffraction (XRD), scanning electron microscopy (SEM), iodometric titration, and variable-temperature conductivity measurements. Four-point probe DC measurements revealed that $CaMnO_{3-\delta}$ (δ = 0.05) has a semiconductive behavior over a temperature range from 25 °C to 300 °C, with its highest conductivity attributed to polaron activity. Cyclic voltammetry (CV) in 0.1 M KOH was employed to assess OER catalytic performance, which correlated with room-temperature conductivity. $CaMnO_{3-\delta}$ exhibited superior catalytic activity, followed by $Ca_{0.5}Sr_{0.5}MnO_{3-\delta}$ and $SrMnO_{3-\delta}$, demonstrating that increased conductivity enhances OER performance. The conductivity trend, $CaMnO_{3-\delta}$ > $Ca_{0.5}Sr_{0.5}MnO_{3-\delta}$ > $SrMnO_{3-\delta}$, aligns with OER activity, underscoring a direct link between electronic transport properties and catalytic efficiency within this series.

Keywords: XRD; solid-state reaction; perovskite oxides; oxygen deficiency; oxygen evolution; conductivity

Academic Editor: Michael T. Timko

Received: 9 December 2024
Revised: 3 January 2025
Accepted: 10 January 2025
Published: 13 January 2025

Citation: Martinson, A.; Guinn, M.; Mortensen, P.; Hona, R.K. Correlation Between Conductivity and Oxygen Evolution Reaction Activity in Perovskite Oxides $CaMnO_{3-\delta}$, $Ca_{0.5}Sr_{0.5}MnO_{3-\delta}$ and $SrMnO_{3-\delta}$. *Sustain. Chem.* **2025**, *6*, 3. https://doi.org/10.3390/suschem6010003

1. Introduction

The development of efficient and stable electrocatalysts for the oxygen evolution reaction (OER) is critical to advancing renewable energy technologies, including water splitting and fuel cell systems. Transition metal oxides, particularly perovskite oxides with the general formula $ABO_{3-\delta}$, have drawn considerable interest as cost-effective alternatives to precious metal catalysts for OER due to their tunable structural, electronic, and catalytic properties. In this study, we investigate three manganese-based perovskite oxides: $CaMnO_{3-\delta}$, $Ca_{0.5}Sr_{0.5}MnO_{3-\delta}$ and $SrMnO_{3-\delta}$. Their structures and properties were vigorously studied before [1,2]. Each of these materials offers a unique configuration of the A-site cation and oxygen vacancy concentration (δ), factors that can significantly influence their electronic structure, conductivity, and ultimately their catalytic activity for OER.

The electronic transport properties of perovskite oxides are closely tied to their catalytic performance. Conductivity in these materials can be affected by factors such as oxygen vacancies, the oxidation state of the transition metal, and structural parameters such as the Mn–O–Mn bond angle. Prior research suggests that oxygen vacancies and charge

transport pathways directly influence OER activity, as higher electronic conductivity can facilitate efficient electron transfer during catalytic reactions [2]. In this work, we focus on the synthesis and characterization of $CaMnO_{3-\delta}$, $Ca_{0.5}Sr_{0.5}MnO_{3-\delta}$ and $SrMnO_{3-\delta}$ to understand how structural and electronic variations impact their OER performance.

We synthesized these oxides via solid-state reactions in air and performed a comprehensive analysis using X-ray diffraction (XRD), scanning electron microscopy (SEM), iodometric titration, and temperature-dependent electrical conductivity measurements. We measured their OER catalytic activity using cyclic voltammetry (CV) in an alkaline medium (0.1 M KOH), where $CaMnO_{3-\delta}$ exhibited superior performance, likely due to its higher conductivity attributed to polaron conduction.

The oxygen evolution reaction (OER) mechanism in alkaline solutions has been extensively studied by various researchers [3,4]. The widely accepted mechanism consists of four steps, each involving a single electron transfer [3,4]. Initially, the reaction begins with the adsorption of hydroxide ions (OH^-) onto the active site of the catalyst, typically a metal site (M) [4]. In the second step, a hydroxide ion from the electrolyte extracts a proton from the M-OH complex, leading to the formation of M-O and water. In the third step, the M-O species reacts with another hydroxide ion to produce a peroxide intermediate. Finally, in the fourth step, this peroxide intermediate interacts with a hydroxide ion, resulting in the formation of oxygen and water, while the catalyst is regenerated [3,4].

1. $M + OH^- \rightarrow M–OH + e^-$
2. $M–OH + OH^- \rightarrow M–O + H_2O + e^-$
3. $M–O + OH^- \rightarrow M–OOH + e^-$
4. $M–OOH + OH^- \rightarrow M + H_2O + O_2 + e^-$

This study highlights the direct correlation between room-temperature conductivity and OER activity, establishing that conductivity plays a pivotal role in enhancing catalytic efficiency. We propose that optimizing the electronic structure and oxygen vacancy content can significantly improve OER performance in perovskite oxide materials. These findings not only contribute to the fundamental understanding of structure–property relationships in manganese-based perovskites but also provide insights for designing effective, non-precious metal OER catalysts.

2. Experimental Method

The materials $CaMnO_{3-\delta}$, $Ca_{0.5}Sr_{0.5}MnO_{3-\delta}$, and $SrMnO_{3-\delta}$ were synthesized in air using a solid-state synthesis method. Precise amounts of $CaCO_3$ (Alfa Aesar, Haverhill, MA, USA, 99.95%), Mn_2O_3 (Alfa Aesar, Haverhill, MA, USA, 99.998%), and $SrCO_3$ (Sigma Aldrich, St. Louis, MO, USA, 99.99%) powders were mixed thoroughly with an agate mortar and pestle. The resulting mixture was pressed into pellets and calcined in air at 1000 °C for 24 h using an MTI furnace. Following calcination, the samples were ground and sintered at 1200 °C for another 24 h under the same atmospheric conditions, with both heating and cooling rates set at 100 °C per hour.

The phase purity and structural properties of the polycrystalline samples were analyzed using powder X-ray diffraction (XRD) at room temperature with a Bruker D2 Phaser diffractometer employing Cu Kα_1 radiation (λ = 1.54056 Å). Rietveld refinements were conducted using GSAS software I [5] with the EXPEGUI interface [6]. Morphological analysis was carried out using high-resolution field-emission scanning electron microscopy (SEM). Electrical properties were assessed via 4-point probe DC measurements on the prepared pellets, with conductivity tested over a temperature range from 25 to 300 °C at a heating rate of 3 °C per minute. Oxygen content in the materials was determined through iodometric titration [7], where approximately 50 mg of each sample was dissolved in 100 mL of 1 M HCl with excess KI (~2 g). A 5 mL aliquot of the solution was titrated

with 0.025 M $Na_2S_2O_3$, and near the endpoint, 0.2 mL of starch solution was added as an indicator. All titration procedures were conducted under an argon atmosphere.

The electrocatalytic performance of the materials was evaluated using a three-electrode electrochemical workstation equipped with a rotating disc electrode set to 1600 rpm. The electrochemical cell consisted of a glassy carbon electrode loaded with the catalyst as the working electrode, a commercial platinum electrode as the counter electrode, and an Ag/AgCl (in 3 M NaCl) electrode as the reference. To prepare the working electrode, a catalyst ink was made by mixing 35 mg of the sample with 20 µL of Nafion solution (5% w/w in water/1-propanol) in 7 mL of tetrahydrofuran (THF), followed by vortex agitation. The resulting suspension was then coated on a glassy carbon electrode of 5 mm diameter or 0.196 cm^2 area by applying four successive layers of 10 µL each. OER measurements were carried out in a 0.1 M KOH electrolyte that was deaerated by purging with argon gas for at 30 min before the CV measurement. CV measurement was accomplished at a scan rate of 10 mV s^{-1} within the potential range of 0 to 0.8 V versus Ag/AgCl.

The potential relative to the reversible hydrogen electrode (RHE) was calculated using the Nernst equation, as follows:

$$E_{RHE} = E_{Ag/AgCl} + 0.059\ pH + E^0{}_{Ag/AgCl} \quad (1)$$

3. Result and Discussion

In the case of perovskite oxides, we can predict the role of ionic radius of A-site cation in the manifestation of the structure of the compounds using the widely accepted following Goldschmidt tolerance factor and ionic radius relation [8]

$$t = \frac{rA + rO}{\sqrt{2}(rB + rO)} \quad (2)$$

where r_A, r_B and r_O are the radius of the A-cation, B-cation, and oxygen. If 't' is greater than 1, the structure would be hexagonal or tetragonal [8–10]. If 't' is between 0.9 and 1, the structure would be cubic [9]. If it is between 0.71 and 9, then the structure would be orthorhombic or rhombohedral, and if 't' falls below 0.71, other different structures could be expected [9,10]. In our case, the A-site cations include Ca, $Ca_{0.5}Sr_{0.5}$ and Sr. Based on the different ionic radii, the structures of these materials are expected to be different.

The crystal structures of the compounds were characterized by the analysis of Powder X-ray diffraction (XRD). $CaMnO_{3-\delta}$ was found to have an orthorhombic structure with *Pnma* space group, as reported before [11]. Figure 1a shows the crystallographic structure of $CaMnO_{3-\delta}$. In the stoichiometric perovskite, $CaMnO_3$, each Mn^{4+} ion is surrounded by six oxygen anions, forming MnO_6 octahedra that share corners with adjacent octahedra. This arrangement creates a three-dimensional network, characteristic of the perovskite structure, where the MnO_6 units are linked together through shared oxygen atoms at their corners. The octahedra are tilted from that of the normal cubic structure, leading to the structural distortion [12]. This distortion can lead to lattice polarization [13,14]. Figure 1b shows the refinement profile and crystal structure of $CaMnO_{3-\delta}$. The refined structural parameters are listed in Table 1. $Ca_{0.5}Sr_{0.5}MnO_{3-\delta}$ shows cubic structure with *Pm*-3*m* space group. Though one report mentioned its structure as orthorhombic with the δ value similar to 0.05, it also mentioned the cubic structure but with δ = 0.02 and 0.25 [15]. In our case, we tried to fit its XRD data with those models mentioned before in the literature [15] but the fitting did not work. Goldschmidt tolerance factor and ionic radius relation can be applicable in such a condition. Figure 2 shows the crystal structure and Rietveld refinement profile of $Ca_{0.5}Sr_{0.5}MnO_{3-\delta}$. The refined structural parameters for this material are listed in Table 2. When Ca in $Ca_{0.5}Sr_{0.5}MnO_{3-\delta}$ is substituted by Sr to get $SrMnO_{3-\delta}$, the crystal

structure transforms from cubic to the hexagonal structure of 4H-$SrMnO_{3-\delta}$. It has $P6_3/mmc$ space group, as reported before [16,17]. Note that all the three materials were prepared in identical conditions. The structure of $SrMnO_{3-\delta}$ is shown in Figure 3. The refined structural parameters for this material are listed in Table 3. Tetravalent Mn occupies the space inside the octahedron. In $SrMnO_{3-\delta}$, oxygen octahedra containing Mn^{4+} ions are organized into face-sharing pairs that are further connected through corner-sharing within the cubically stacked "A" layers. This compound is notable for exhibiting both cubic and hexagonal polymorphs, making it a rare example in the family of perovskite oxides. The structural flexibility between cubic and hexagonal forms is influenced by the oxygen deficiency (δ), which plays a significant role in determining the polymorphic form of $SrMnO_{3-\delta}$.

Table 1. Refined structural parameters for CaMnO3-δ using powder X-ray diffraction data; Space group: *Pnma*, *a* = 5.2864(4) Å, b = 7.4634(5) Å, c = 5.2714(4) Å, V = 53.889(6) Å^3, Rp = 0.047, wRp = 0.059, χ^2 = 1.112.

Element	x	y	z	Uiso	Occupancy	Multiplicity
O1	0.4969(31)	0.25	0.071(4)	0.012(7)	1	4
O2	0.294(2)	0.030(3)	0.718(3)	0.005(4)	1	8
Mn1	0.0	0.0	0.5	0.002(1)	1	4
Ca1	0.033(1)	0.25	−0.006(3)	0.007(2)	1	4

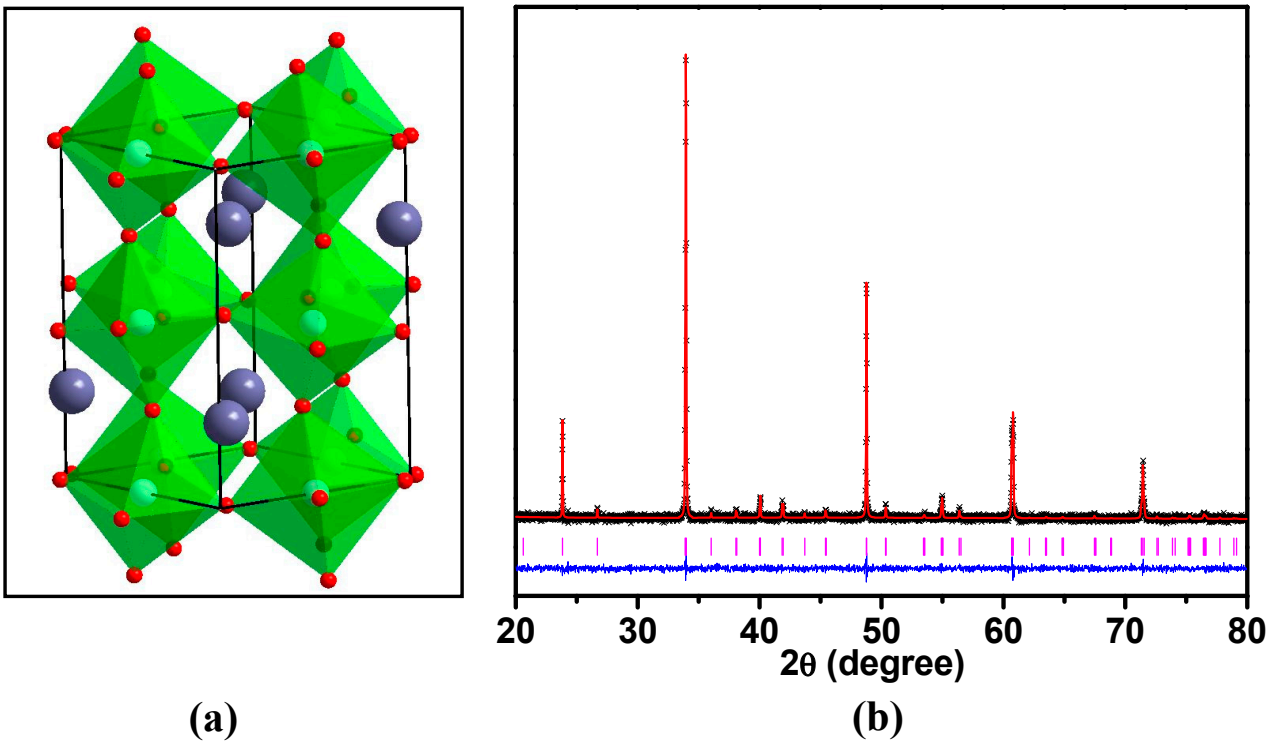

Figure 1. $CaMnO_{3-\delta}$ (**a**) crystallographic structure with unit cell, (**b**) Reitveld refinement profile for the PXRD.

Table 2. Refined structural parameters for $CaSrMnO_{3-\delta}$ using powder X-ray diffraction data; space group: *Pm-3m*, *a* = 3.7771(1) Å, V = 53.886 Å^3, Rp = 0.0506, wRp = 0.0632, χ^2 = 1.370.

Element	x	y	z	Uiso	Occupancy	Multiplicity
Ca1	0.5	0.5	0.5	0.025(2)	0.5	1
Sr1	0.5	0.5	0.5	0.025(2)	0.5	1
Mn1	0.0	0.0	0.0	0.036(3)	1	1
O1	0.5	0.5	0.0	0.068(3)	0.9867	3

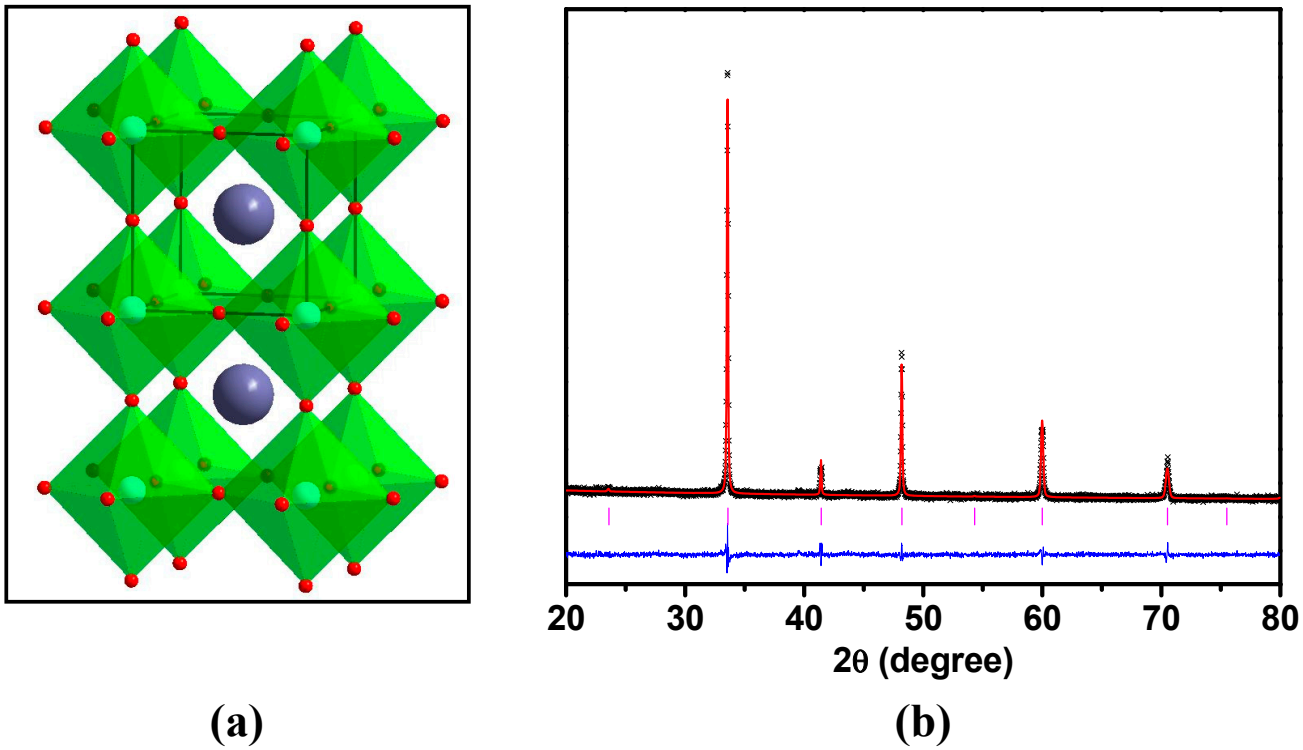

Figure 2. $Ca_{0.5}Sr_{0.5}MnO_{3-\delta}$ (**a**) crystallographic structure with unit cell, (**b**) Reitveld refinement profile for the PXRD.

In $SrMnO_{3-\delta}$, the Mn-O bond distances exhibit significant variation, measured at 1.81, 1.87, 1.91, and 2.03 Å, which can be attributed to the dual types of polyhedral connectivity: face-sharing and corner-sharing. While a direct comparison of bond distances across the compounds $SrMnO_{3-\delta}$, $CaMnO_{3-\delta}$, and $Ca_{0.5}Sr_{0.5}MnO_{3-\delta}$ is not entirely appropriate due to their structural differences, it is observed that the average Mn-O bond distance in $SrMnO_{3-\delta}$ (1.91 Å) is slightly longer than in $CaMnO_{3-\delta}$ and $Ca_{0.5}Sr_{0.5}MnO_{3-\delta}$ (1.89 Å). Additionally, the Mn-O-Mn bond angles in $SrMnO_{3-\delta}$ reflect the structural variations, with angles as small as 80.9(3)° in the face-sharing octahedral dimers, whereas the corner-sharing octahedra exhibit a larger Mn-O-Mn bond angle of 166(1)° [2]. However, $Ca_{0.5}Sr_{0.5}MnO_{3-\delta}$ contains only one type of Mn-O-Mn angle, which is 180°, as expected from a cubic perovskite structure. In the case of $CaMnO_{3-\delta}$, the average Mn-O-Mn angle remains 180°, but the tetrahedral geometries are regularly tilted to cause structural destruction which is believed to create lattice polarization and polarons in the compound [12,13,18,19].

Table 3. Refined structural parameters for $SrMnO_{3-\delta}$ using powder X-ray diffraction data; space group: $P6_3/mmc$, a = 5.4549(8) Å, b = 5.4549(8) Å, c = 9.0905(8) Å, V = 270.496 $Å^3$, Rp = 0.0529, wRp = 0.0699, χ^2 = 1.890.

Element	x	y	z	Uiso	Occupancy	Multiplicity
Sr1	0.0	0.0	−0.197(7)	0.020(6)	0.5	4
Sr2	0.333(3)	0.666(7)	0.250	0.020(6)	1	2
Mn1	0.333(3)	0.666(7)	0.572(7)	0.031(4)	1	4
O1	0.5	0.0	0.0	0.020(6)	0.9000	6
O2	−0.898055	0.898055	0.750000	0.020(6)	0.9000	6

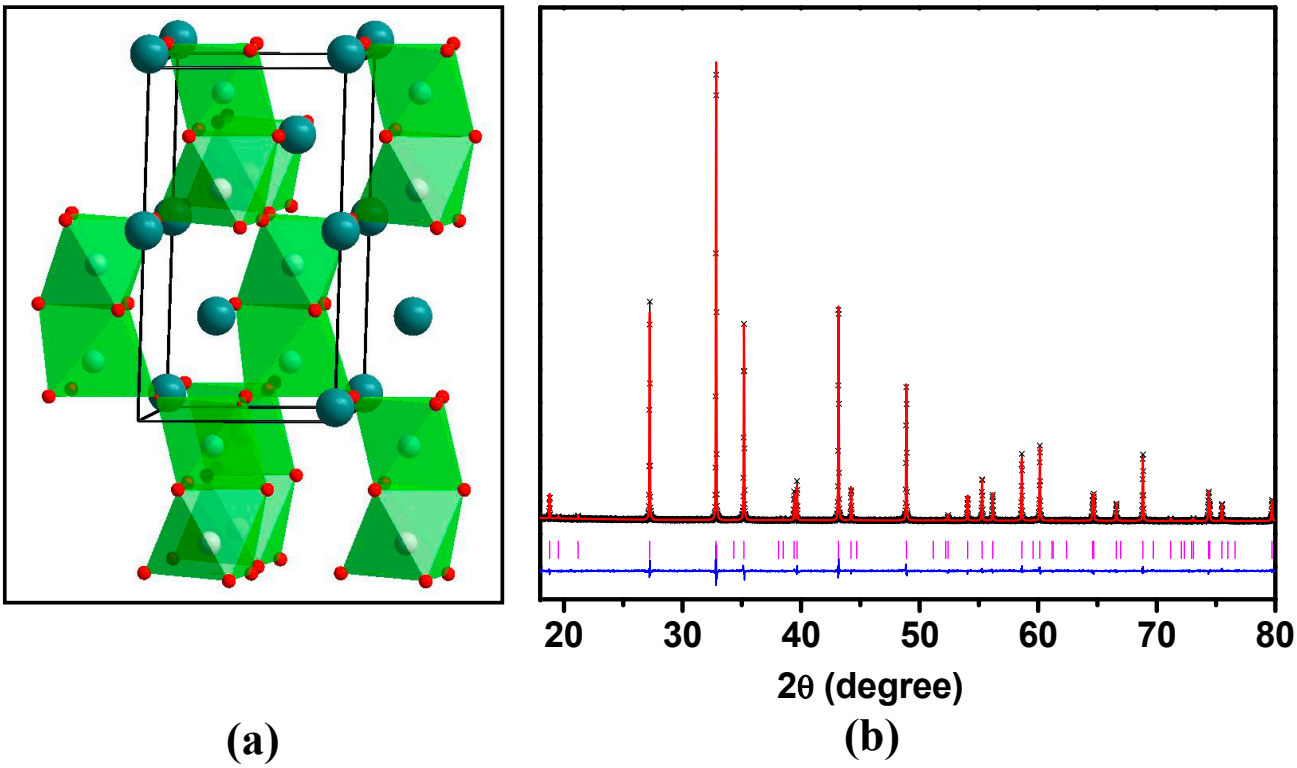

Figure 3. $SrMnO_{3-\delta}$ (**a**) crystallographic structure with unit cell, (**b**) Reitveld refinement profile for the PXRD.

The morphology and grain sizes of all the three materials (Ca_2, CaSr and Sr_2) were analyzed using scanning electron microscopy (SEM). Figure 4 presents the SEM images of the sintered pellets for each material, highlighting the surface morphology and grain structure. These images provide insights into the grain size and distribution, which are crucial for understanding the material's microstructural properties and their potential impact on electrical and catalytic performance. It seems that the grain sizes are the smallest for $SrMnO_{3-\delta}$. $Ca_{0.5}Sr_{0.5}MnO_{3-\delta}$ shows the diffused crystallites. From the SEM images, it seems that the grain size decreases with the increase in the average A-site cationic radius in this series. Note that the ionic radius of Ca is the smallest. It shows that the structural morphology is also affected by the average ionic radius of A-site cations. The bigger the average ionic radius, the smaller the crystallite size. All the materials look porous in the SEM images.

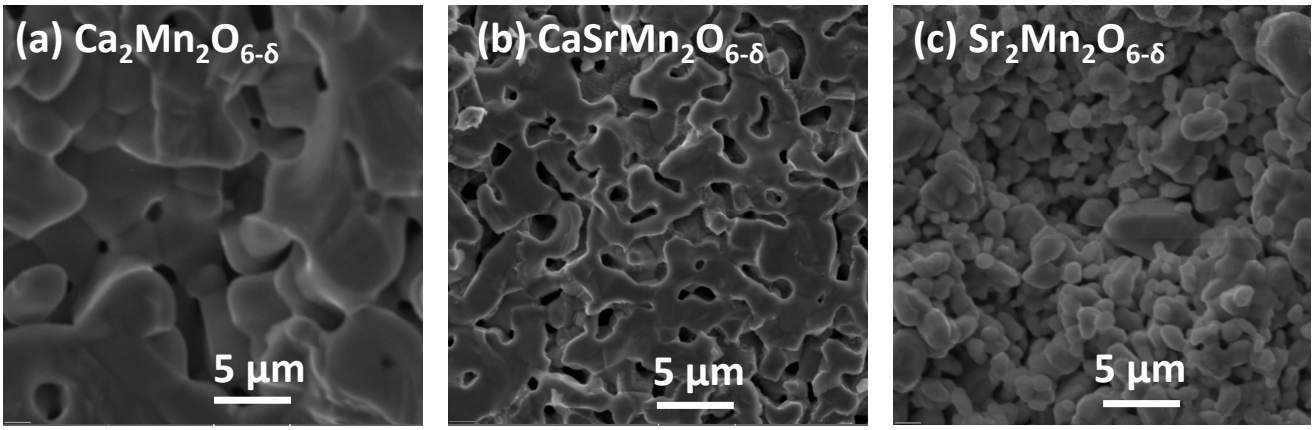

Figure 4. Scanning electron microscopy images of $CaMnO_{3-\delta}$ (**a**), $Ca_{0.5}Sr_{0.5}MnO_{3-\delta}$ (**b**), and $SrMnO_{3-\delta}$ (**c**) from left to right.

Iodometric titration shows the δ value 0.05, 0.05, and 0.0 for $CaMnO_{3-\delta}$, $Ca_{0.5}Sr_{0.5}MnO_{3-\delta}$ and $SrMnO_{3-\delta}$, respectively, which show that all materials contain almost all Mn in 4+ oxidation state. These values are similar to those of previous reports [11,15,16,20].

3.1. Electrical Conductivity

The study of the electrical properties of these materials was performed by the four-point probe technique through direct current (DC) measurement. In the DC method, the output current (I) is measured by applying a constant voltage (V), and the resistance (R) is determined using Ohm's law:

$$R = \frac{V}{I} \tag{3}$$

The resistance values obtained are then used to calculate the electrical conductivity (σ) using the equation [21]:

$$\sigma = \frac{1}{R} \times \frac{L}{A} \tag{4}$$

where L and A represent the voltage probe spacing and cross-sectional area of the pellet from where current passes, respectively. The electrical conductivities of the compounds were also obtained at different temperatures from 25 to 300 °C. Throughout the studied temperatures, the electrical conductivity of the Ca—material is the highest while that of the Sr—material is the lowest with the conductivity order of $CaMnO_{3-\delta} > Ca_{0.5}Sr_{0.5}MnO_{3-\delta} > SrMnO_{3-\delta}$. Figure 5 shows the conductivity of the materials at room temperature through 300 °C.

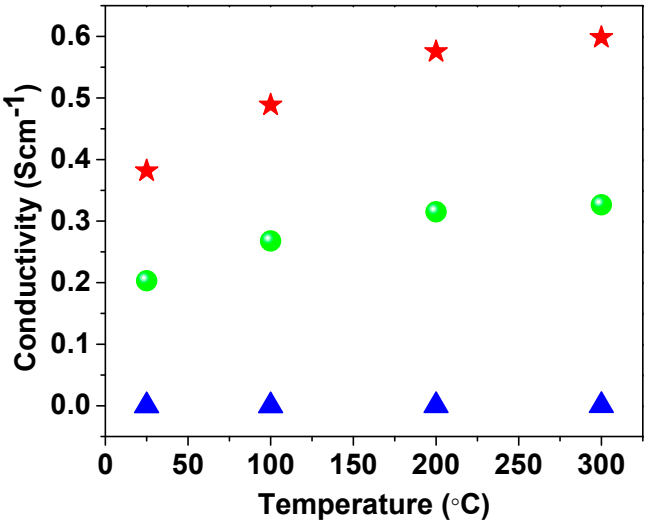

Figure 5. Temperature-dependent total electrical conductivity of $CaMnO_{3-\delta}$ (red stars), $Ca_{0.5}Sr_{0.5}MnO_{3-\delta}$ (green spheres), and $SrMnO_{3-\delta}$ (blue triangles).

Perovskite oxides have transition metal cations at B-site. Generally, these B-site cations have flexible multiple oxidation states such as Mn^{3+}/Mn^{4+}. When there are different oxidation states of B-site cations in a compound, electrons hop from one cation to another through M^{m+}-O-M^{n+} bond system resulting into electrical conduction [22,23]. However, there are reports for perovskite oxides which do not possess B-site cation with multiple or different oxidation states [24]. Still it demonstrates the electrical conductivity, though very small in magnitude. Our compounds are also of similar type where the B-site cation do not possess significant multiple oxidation states. Ca_2 material has structure distorted from regular cubic structure where octahedra are tilted [12]. This structural distortion can lead to lattice polarization [13,14,19]. This lattice polarization is responsible for the formation of small polarons in the crystal [19,25]. These polarons are responsible for the electrical

conductivity at room temperature [19,25]. These types of small polarons due to structural distortion are not formed in CaSr and Sr_2 material. Hence, Ca_2 material has the highest conductivity at room temperature. The oxygen content play significant role in conductivity as it determines the concentration of M^{m+}-O-M^{n+} bond systems in a compound. The δ values for Ca_2, CaSr and Sr_2, materials are 0.05, 0.05, and 0.00, respectively.

CaSr material has 180^0 of Mn-O-Mn bond angles while Sr_2 material has a lower bond angle because of the face sharing. Since M-O bond is formed by the overlap of Mn-3d orbital with O-2p orbital, larger M-O-M bond angles have better orbital overlap which leads to better conductivity [26]. The shorter the M-O bond distance, the greater the orbital overlap and the wider the conduction band which makes the material more conductive [26]. Thus, the Sr_2 material has the lowest room temperature conductivity (almost zero) due to nil Mn^{3+}/Mn^{4+} ratio and the smaller bond angle.

We also studied the temperature dependent conductivity of these materials. Figure 5 shows the temperature dependent electrical conductivity of the three materials. The conductivity measurement of the three materials at different temperatures exhibits increasing conductivity with the rise of temperature. It indicates the semiconductive nature of the materials. In such perovskite oxide materials, which show the semiconductor type conductivity, the materials demonstrate the loss of oxygen with the rise in temperature [27,28]. Most of the Mn remains in 4+ oxidation state before the loss of oxygen to balance the overall charge of the stoichiometric compound. When oxygen is lost due to heat, some Mn^{4+} get reduced to Mn^{3+} forming Mn^{3+}-O-Mn^{4+} conduction pathways. Thus, the conduction pathways Mn^{3+}-O-Mn^{4+} increase with the rise of temperature [29,30]. The charge transport mechanism can be expressed by Kroger–Vink notations. The loss of oxygen produces oxygen vacancies [29].

The Kroger and Vink equations are surprising: in a theoretical solid solution classically expressed as:

$Ca(^{2+})Mn(^{4+})_{(1-y)}\ Mn(^{3+})_{(y)}\ O(^{2-})_{(3-x)}\ V_{O\ (x)}$

we should have the relation: y = 2x.

$2Mn^{4+} + è \rightarrow 2\ Mn^{3+} + 2h^{\bullet}$

$2\ h^{\bullet} + O^{X} + è \rightarrow ½\ O_2\ (gas) + V^{\bullet\bullet}$

The equation according to K and V would therefore be written using the doubly charged vacancy $V^{\bullet\bullet}$:

$2\ Mn^{X} + O^{X} ==> 2\ Mn' + 1/2\ O_2\ (gas) + V_o^{\bullet\bullet}$.

Here, O^x, $V_o^{\bullet\bullet}$ and $h^{\bullet}$ represent lattice oxygen, oxygen vacancy, and hole, respectively. As the temperature increases, the process of formation and consumption of the holes increases with the increase of the concentration of the oxygen vacancies due to increased oxygen loss. These holes are responsible for p-type conductivity [29,30]. Hole mobility increases with the temperature rise. The relation between the conductivity and the mobility of the charge carrier for temperature-activated conductivity can be represented as

$$\sigma = ne\mu \quad (5)$$

where σ, n, e, and μ are the conductivity, concentration of electrons/holes, charge of the electron, and mobility of the charge carriers, respectively.

3.2. Correlation Between OER and Conductivity

Many perovskite oxides have shown electrocatalytic activity toward OER [31,32]. We also investigated the electrocatalytic activity of these materials for OER, to see the relation of their conductive nature with catalytic activity. The OER activities of the three materials were studied by cyclic voltammetry. For oxygen evolution reaction (OER) measurements, numerous studies have incorporated carbon black into the electrode composition to im-

prove electrical conductivity and optimize the catalyst's utilization. The addition of carbon black helps facilitate efficient charge transfer within the electrode, thereby enhancing the overall performance of the OER process [33–35]. However, recent studies have revealed that carbon plays a more intricate role beyond merely serving as a conductive support. It can actively participate in the catalytic process, influence the electrochemical environment, and interact with the catalyst, potentially affecting its activity and stability during the oxygen evolution reaction (OER). These findings suggest that carbon's role in OER is multifaceted, contributing to both the physical and chemical properties of the electrode [36,37]. For example, X-ray absorption near-edge spectroscopy study of $Ba_{0.5}Sr_{0.5}Co_{0.8}Fe_{0.2}O_3$/carbon composite electrode demonstrated the reduction of Co during the composite preparation process [38]. for this reason, some researchers have studied OER without carbon black [26]. We also followed the OER experiments without carbon black. It has been found that CaSr material shows intermediate onset potential (~1.6 eV) for oxygen generation, while the Ca and Sr material show the lowest (~1.54 eV) and largest (~1.68) onset potential, respectively. However, these catalysts are inferior to RuO_2 or IrO_2.

The mass activity (A/g) was also calculated for $CaMnO_{3-\delta}$, $Ca_{0.5}Sr_{0.5}MnO_{3-\delta}$ and $SrMnO_{3-\delta}$. This was done using the catalyst loading mass (0.1 mg_{cat} $cm_{GEO}{}^{-2}$) and the measured current density J (mA $cm_{GEO}{}^{-2}$). The inset in Figure 6a compares the OER mass activity of the three materials at 1.80 V vs. RHE. The CaSr material shows the intermediate mass activity (0.42 A/g), while the Ca and Sr material show the largest (1.1 A/g) and lowest (0.28 A/g) mass activity toward OER, respectively.

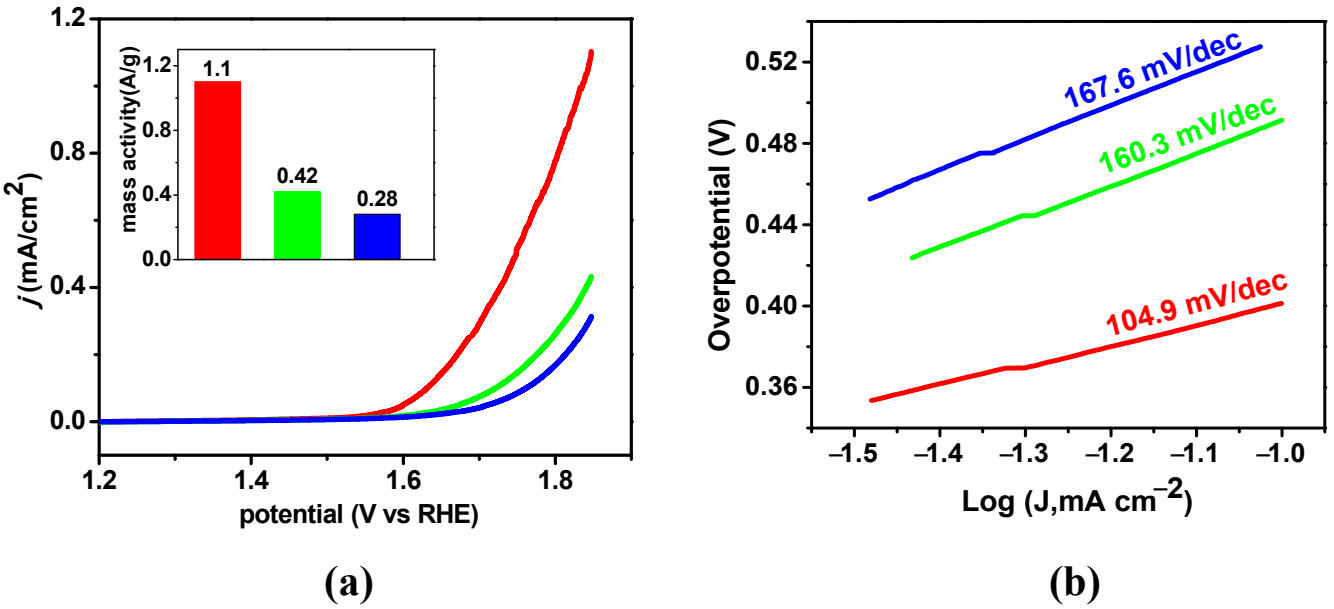

Figure 6. (**a**) Polarization curves of OER with the mass activities in inset and (**b**) Tafel slope for $CaMnO_3$ (red), $Ca_{0.5}Sr_{0.5}MnO_{3-\delta}$ (green) and $SrMnO_3$ (blue).

The Tafel slope is commonly used to study the kinetics of the oxygen evolution reaction (OER) and is evaluated using the Tafel equation: [39,40]

$$\eta = a + b \log j \quad (6)$$

where η is the overpotential, and j is the current density. The Tafel plot (η vs. log j) provides insights into both electron and mass transport, reflecting the efficiency of the electrocatalyst's activity [41,42]. A lower Tafel slope typically indicates faster reaction kinetics and enhanced OER performance [42]. The Tafel slopes for $CaMnO_{3-\delta}$, $Ca_{0.5}Sr_{0.5}MnO_{3-\delta}$ and

$SrMnO_{3-\delta}$ are found to be 104.9 mV/dec, 160.3 mV/dec, and 167.4 mV/dec, respectively, as shown in Figure 6b. Among these, $CaMnO_{3-\delta}$ exhibits the lowest Tafel slope, correlating with its superior OER activity, suggesting that it facilitates more efficient charge transfer compared to the other materials. Similarly, $Ca_{0.5}Sr_{0.5}MnO_{3-\delta}$ and $SrMnO_{3-\delta}$ show intermediate and the highest Tafel slope. Since $CaMnO_{3-\delta}$ presents the superior performance, its stability was tested in terms of CV cycles. It is stable only up to 20 cycles.

These OER experiments show the trend of the comparative catalytic activity as $CaMnO_{3-\delta} > Ca_{0.5}Sr_{0.5}MnO_{3-\delta} > SrMnO_{3-\delta}$. Note that the conductivity trend also follows the same direction as $CaMnO_{3-\delta} > Ca_{0.5}Sr_{0.5}MnO_{3-\delta} > SrMnO_{3-\delta}$. It shows the correlation between conductivity and OER catalytic activity.

4. Conclusions

The structure of $AMnO_{3-\delta}$ transforms from orthorhombic through cubic to hexagonal as Ca decreases and Sr increases. $CaMnO_{3-\delta}$ is orthorhombic, $Ca_{0.5}Sr_{0.5}MnO_{3-\delta}$ is cubic and $SrMnO_{3-\delta}$ is hexagonal. $CaMnO_{3-\delta}$ has the highest conductivity due to polaron activity and $SrMnO_{3-\delta}$ has the lowest conductivity due to the absence of oxygen vacancy and the smallest Mn-O-Mn bond angle or structural effect. Their electrocatalytic activity toward OER demonstrated the catalytic performance order as $CaMnO_{3-\delta} > Ca_{0.5}Sr_{0.5}MnO_{3-\delta} > SrMnO_{3-\delta}$ in terms of onset and mass activity. This trend follows the same trend of conductivity, showing the direct relation between conductivity and OER catalytic activity in the series of materials.

Author Contributions: Conceptualization, R.K.H.; Methodology, A.M. and R.K.H.; Resources, M.G.; Writing—review & editing, R.K.H.; Project administration, P.M.; Funding acquisition, M.G. All authors have read and agreed to the published version of the manuscript.

Funding: This work is partly supported by the National Science Foundation Tribal College and University Program Instructional Capacity Excellence in TCUP Institutions (ICE-TI) grant award #2225648. A part of this work is supported by NSF TCUP Tribal Enterprise Advancement Center grant no. HRD 1839895. A part of the work is supported by AIHEC-coordinated NASA TCU Building Bridges, Grant Number 80NSSC24M0025. Additional support for the work came from ND EPSCOR STEM equipment grants. Permission was granted by the United Tribes Technical Colleges (UTTC) Environmental Science Department to publish this information. The views expressed are those of the authors and do not necessarily represent those of United Tribes Technical College.

Institutional Review Board Statement: Not applicable.

Informed Consent Statement: Not applicable.

Data Availability Statement: Data is available upon request.

Conflicts of Interest: The authors declare no conflicts of interest.

References

1. Chang, L.; Li, J.; Le, Z.; Nie, P.; Guo, Y.; Wang, H.; Xu, T.; Xue, X. Perovskite-type CaMnO3 anode material for highly efficient and stable lithium ion storage. *J. Colloid Interface Sci.* **2021**, *584*, 698–705. [CrossRef] [PubMed]
2. Hona, R.K.; Ramezanipour, F. Structure-dependence of electrical conductivity and electrocatalytic properties of $Sr_2Mn_2O_6$ and $CaSrMn_2O_6$. *J. Chem. Sci.* **2019**, *131*, 109. [CrossRef]
3. Zhu, Y.; Zhou, W.; Sunarso, J.; Zhong, Y.; Shao, Z. Phosphorus-Doped Perovskite Oxide as Highly Efficient Water Oxidation Electrocatalyst in Alkaline Solution. *Adv. Funct. Mater.* **2016**, *26*, 5862–5872. [CrossRef]
4. Rong, X.; Parolin, J.; Kolpak, A.M. A Fundamental Relationship between Reaction Mechanism and Stability in Metal Oxide Catalysts for Oxygen Evolution. *ACS Catal.* **2016**, *6*, 1153–1158. [CrossRef]
5. Larson, A.C.; Von Dreele, A.C. *General Structure Analysis System (GSAS)*; Los Alamos National Laboratory Report LAUR; Los Alamos National Laboratory: Los Alamos, NM, USA, 1994; pp. 86–748.
6. Toby, B.H. EXPGUI, a graphical user interface for GSAS. *J. Appl. Crystallogr.* **2001**, *34*, 210–213. [CrossRef]

7. Hona, R.K.; Ramezanipour, F. Disparity in electrical and magnetic properties of isostructural oxygen-deficient perovskites $BaSrCo_2O_{6-\delta}$ and $BaSrCoFeO_{6-\delta}$. *J. Mater. Sci. Mater. Electron.* **2018**, *29*, 13464–13473. [CrossRef]
8. Galinsky, N.; Sendi, M.; Bowers, L.; Li, F. $CaMn_{1-x}B_xO_{3-\delta}$ (B=Al, V, Fe, Co, and Ni) perovskite based oxygen carriers for chemical looping with oxygen uncoupling (CLOU). *Appl. Energy* **2016**, *174*, 80–87. [CrossRef]
9. Sato, T.; Takagi, S.; Deledda, S.; Hauback, B.C.; Orimo, S.-I. Extending the applicability of the Goldschmidt tolerance factor to arbitrary ionic compounds. *Sci. Rep.* **2016**, *6*, 23592. [CrossRef]
10. Roth, R.S. Classification of perovskite and other ABO_3-type compounds. *J. Res. Natl. Bur. Stand.* **1957**, *58*, 75. [CrossRef]
11. Taguchi, H.; Nagao, M.; Sato, T.; Shimada, M. High-temperature phase transition of $CaMnO_{3-\delta}$. *J. Solid State Chem.* **1989**, *78*, 312–315. [CrossRef]
12. Aschauer, U.; Pfenninger, R.; Selbach, S.M.; Grande, T.; Spaldin, N.A. Strain-controlled oxygen vacancy formation and ordering in $CaMnO_3$. *Phys. Rev. B* **2013**, *88*, 054111. [CrossRef]
13. Tilley, R.J.D. *Defects in Solids*; John Wiley & Sons, Inc.: Hoboken, NJ, USA, 2008.
14. Asenath-Smith, E.; Misture, S.T.; Edwards, D.D. Structural behavior and thermoelectric properties of the brownmillerite system $Ca_2(ZnxFe_{2-x})O_5$. *J. Solid State Chem.* **2011**, *184*, 2167–2177. [CrossRef]
15. Töpfer, J.; Pippardt, U.; Voigt, I.; Kriegel, R. Structure, nonstoichiometry and magnetic properties of the perovskites $Sr_{1-x}Ca_xMnO_{3-\delta}$. *Solid State Sci.* **2004**, *6*, 647–654. [CrossRef]
16. Belik, A.A.; Matsushita, Y.; Katsuya, Y.; Tanaka, M.; Kolodiazhnyi, T.; Isobe, M.; Takayama-Muromachi, E. Crystal structure and magnetic properties of 6H-$SrMnO_3$. *Phys. Rev. B* **2011**, *84*, 094438. [CrossRef]
17. Søndenå, R.; Ravindran, P.; Stølen, S.; Grande, T.; Hanfland, M. Electronic structure and magnetic properties of cubic and hexagonal $SrMnO_3$. *Phy. Rev. B* **2006**, *74*, 144102. [CrossRef]
18. Asenath-Smith, E.; Lokuhewa, I.N.; Misture, S.T.; Edwards, D.D. p-Type thermoelectric properties of the oxygen-deficient perovskite $Ca_2Fe_2O_5$ in the brownmillerite structure. *J. Solid State Chem.* **2010**, *183*, 1670–1677. [CrossRef]
19. Durán, A.; Verdin, E.; Escamilla, R.; Morales, F.; Escudero, R. Mechanism of small-polaron formation in the biferroic $YCrO_3$ doped with calcium. *Mater. Chem. Phys.* **2012**, *133*, 1011–1017. [CrossRef]
20. Du, J.; Zhang, T.; Cheng, F.; Chu, W.; Wu, Z.; Chen, J. Nonstoichiometric perovskite $CaMnO_{3-\delta}$ for oxygen electrocatalysis with high activity. *Inorg. Chem.* **2014**, *53*, 9106–9114. [CrossRef]
21. Singh, Y. Electrical Resistivity Measurements: A Review. *Int. J. Modern Phys. Conf. Ser.* **2013**, *22*, 745–756. [CrossRef]
22. Zhang, Q.; Xu, Z.; Wang, L.; Gao, S.; Yuan, S. Structural and electromagnetic properties driven by oxygen vacancy in $Sr_2FeMoO_{6-\delta}$ double perovskite. *J. Alloys Compd.* **2015**, *649*, 1151–1155. [CrossRef]
23. Kozhevnikov, V.L.; Leonidov, I.A.; Mitberg, E.B.; Patrakeev, M.V.; Petrov, A.N.; Poeppelmeier, K.R. Conductivity and carrier traps in $La_{1-x}SrxCo_{1-z}Mn_zO_{3-\delta}$ (x = 0.3; z = 0 and 0.25). *J. Solid State Chem.* **2003**, *172*, 296–304. [CrossRef]
24. Hona, R.K.; Huq, A.; Ramezanipour, F. Magnetic structure of $CaSrFeCoO_{6-\delta}$: Correlations with structural order. *Mater. Res. Bull.* **2018**, *106*, 131–136. [CrossRef]
25. Kao, K.C. *Dielectric Phenomena in Solids*; Academic Press: Cambridge, MA, USA, 2004; p. 402, ISBN 0-12-396561-6.
26. Cheng, X.; Fabbri, E.; Nachtegaal, M.; Castelli, I.E.; El Kazzi, M.; Haumont, R.; Marzari, N.; Schmidt, T.J. Oxygen evolution reaction on $La_{1-x}Sr_xCoO_3$ perovskites: A combined experimental and theoretical study of their structural, electronic, and electrochemical properties. *Chem. Mater.* **2015**, *27*, 7662–7672. [CrossRef]
27. Hona, R.K.; Huq, A.; Ramezanipour, F. Unraveling the Role of Structural Order in the Transformation of Electrical Conductivity in $Ca_2FeCoO_{6-\delta}$, $CaSrFeCoO_{6-\delta}$, and $Sr_2FeCoO_{6-\delta}$. *Inorg. Chem.* **2017**, *56*, 14494–14505. [CrossRef]
28. Hona, R.K.; Huq, A.; Mulmi, S.; Ramezanipour, F. Transformation of Structure, Electrical Conductivity, and Magnetism in $AA'Fe_2O_{6-\delta}$, A = Sr, Ca and A′ = Sr. *Inorg. Chem.* **2017**, *56*, 9716–9724. [CrossRef]
29. Yáng, Z.; Harvey, A.S.; Infortuna, A.; Schoonman, J.; Gauckler, L.J. Electrical conductivity and defect chemistry of $Ba_xSr_{1-x}Co_yFe_{1-y}O_{3-\delta}$ perovskites. *J. Solid State Electrochem.* **2011**, *15*, 277–284. [CrossRef]
30. Patrakeev, M.V.; Leonidov, I.A.; Kozhevnikov, V.L.; Poeppelmeier, K.R. p-Type electron transport in $La_{1-x}Sr_xFeO_{3-\delta}$ at high temperatures. *J. Solid State Chem.* **2005**, *178*, 921–927. [CrossRef]
31. Lee, J.G.; Hwang, J.; Hwang, H.J.; Jeon, O.S.; Jang, J.; Kwon, O.; Lee, Y.; Han, B.; Shul, Y.G. A new family of perovskite catalysts for oxygen-evolution reaction in alkaline media: $BaNiO_3$ and $BaNi_{0.83}O_{2.5}$. *J. Am. Chem. Soc.* **2016**, *138*, 3541–3547. [CrossRef]
32. Kim, J.; Yin, X.; Tsao, K.; Fang, S.; Yang, H. $Ca_2Mn_2O_5$ as oxygen-deficient perovskite electrocatalyst for oxygen evolution reaction. *J. Am. Chem. Soc.* **2014**, *136*, 14646–14649. [CrossRef]
33. Jin, C.; Cao, X.; Zhang, L.; Zhang, C.; Yang, R. Preparation and electrochemical properties of urchin-like $La_{0.8}Sr_{0.2}MnO_3$ perovskite oxide as a bifunctional catalyst for oxygen reduction and oxygen evolution reaction. *J. Power Sources* **2013**, *241*, 225–230. [CrossRef]
34. May, K.J.; Carlton, C.E.; Stoerzinger, K.A.; Risch, M.; Suntivich, J.; Lee, Y.-L.; Grimaud, A.; Shao-Horn, Y. Influence of oxygen evolution during water oxidation on the surface of perovskite oxide catalysts. *J. Phys. Chem. Lett.* **2012**, *3*, 3264–3270. [CrossRef]

35. Malkhandi, S.; Trinh, P.; Manohar, A.K.; Jayachandrababu, K.C.; Kindler, A.; Prakash, G.S.; Narayanan, S.R. Electrocatalytic activity of transition metal oxide-carbon composites for oxygen reduction in alkaline batteries and fuel cells. *J. Electrochem. Soc.* **2013**, *160*, 943–952. [CrossRef]
36. Liang, Y.; Li, Y.; Wang, H.; Zhou, J.; Wang, J.; Regier, T.; Dai, H. Co_3O_4 nanocrystals on graphene as a synergistic catalyst for oxygen reduction reaction. *Nat. Mater.* **2011**, *10*, 780–786. [CrossRef]
37. Mohamed, R.; Cheng, X.; Fabbri, E.; Levecque, P.; Kötz, R.; Conrad, O.; Schmidt, T.J. Electrocatalysis of perovskites: The influence of carbon on the oxygen evolution activity. *J. Electrochem. Soc.* **2015**, *162*, 579–586. [CrossRef]
38. Fabbri, E.; Nachtegaal, M.; Cheng, X.; Schmidt, T.J. Superior bifunctional electrocatalytic activity of $Ba_{0.5}Sr_{0.5}Co_{0.8}Fe_{0.2}O_{3-\delta}$/carbon composite electrodes: Insight into the local electronic structure. *Adv. Energy Mater.* **2015**, *5*, 1402033. [CrossRef]
39. Pan, Y.; Chen, Y.; Li, X.; Liu, Y.; Liu, C. Nanostructured nickel sulfides: Phase evolution, characterization and electrocatalytic properties for the hydrogen evolution reaction. *RSC Adv.* **2015**, *5*, 104740–104749. [CrossRef]
40. Oh, S.; Kim, H.; Kwon, Y.; Kim, M.; Cho, E.; Kwon, H. Porous Co–P foam as an efficient bifunctional electrocatalyst for hydrogen and oxygen evolution reactions. *J. Mater. Chem. A* **2016**, *4*, 18272–18277. [CrossRef]
41. Song, F.; Hu, X. Ultrathin cobalt–manganese layered double hydroxide Is an efficient oxygen evolution catalyst. *J. Am. Chem. Soc.* **2014**, *136*, 16481–16484. [CrossRef]
42. Moir, J.; Soheilnia, N.; O'brien, P.; Ali, F.M.; Grozea, C.M.; Faulkner, D.; Helander, M.G.; Ozin, G.A. Enhanced hematite water electrolysis using a 3D antimony-doped tin oxide electrode. *ACS Nano* **2013**, *7*, 4261–4274. [CrossRef]